(3+1)-dimensional numerical simulations of femtosecond laser filaments in air: Toward a quantitative agreement with experiments

S. Champeaux* and L. Bergé
Commissariat à l'Énergie Atomique, Centre DAM-Ile de France, Département de Physique Théorique et Appliquée, Bruyères-le-Châtel, 91297 Arpajon Cedex, France

D. Gordon, A. Ting, J. Peñano, and P. Sprangle
Plasma Physics Division, Naval Research Laboratory, Washington, D.C. 20375, USA
(Received 24 September 2007; revised manuscript received 19 December 2007; published 13 March 2008)

Three-dimensional numerical simulations and direct experimental measurements of the multifilamentation of femtosecond laser pulses propagating in air are quantitatively compared. Agreement is obtained in terms of the evolution of the filamentation pattern and in terms of the size and energy of the individual filaments through 12 m of propagation. These results are made possible by the combination of a massively parallel propagation code along with a nondestructive experimental diagnostic technique. Influence of the pulse duration is moreover addressed. The numerical calculations also show that single and multiple filaments exhibit almost identical spectral signature.

DOI: 10.1103/PhysRevE.77.036406 PACS number(s): 52.38.Hb, 42.65.Jx, 42.65.Tg, 42.68.Ay

I. INTRODUCTION

Nonlinear propagation of ultrashort pulses in air has been a subject of broad interest for the past several years [1]. If the peak power exceeds the critical power for self-focusing, beam natural diffraction is overcome by Kerr self-focusing. The pulse therefore undergoes spatial and temporal narrowing [2], followed by pulse splitting and plasma defocusing induced by photoionization of air molecules [3]. The dynamical equilibrium between Kerr compression and plasma generation allows the pulse to self-channel over long distances in the form of micrometric filaments coupled with tenuous plasma channels. For infrared pulses, the filaments reach high intensity of a few tens of $\mathrm{TW/cm^2}$ clamped with an averaged electron density of the order of 10^{16} $\mathrm{cm^{-3}}$. The critical power is one of the key parameters in the filamentation process. Knowledge of the magnitude of the nonlinear Kerr index is thus crucial. If the input peak power does not exceed a few tens of critical powers, one or a few filaments are created. At powers far above critical, multiple filaments emerge after a stage of modulational instability and can maintain the beam in focused state upon large propagation ranges, through the persistence of filamentary clusters. Those properties as well as the large white light spectrum developed by the pulse find direct applications in remote sensing and lightning control technologies [4]. Numerical models with varying levels of sophistication were shown to successfully capture the phenomenology of atmospheric self-channeling. Till recently, agreement with experiments was only met on qualitative grounds. Regarding single filamentation, Kerr focusing, plasma defocusing along with optical shocks compete in strongly reshaping the pulse temporal profile. The sharp trail following the leading peak formation has been shown to be responsible for a prominent blueshift in the pulse spectrum, which explains the observed white-light continuum generated in air [5]. Among the first attempts toward quantitative agreements between theoretical predictions and experimental measurements, we can mention the results obtained by Pitts *et al.* for subcritical propagation over nearly 23 m in air [6]. Time has come to reach similar fidelity between numerical and experimental multifilamented beams. Besides the subtle balance between the nonlinear processes which give rise to a single filament, multifilamentation implies a more complex dynamics due to the coupling between spatial and temporal distortions, producing optically turbulent patterns [7]. The actual performances of computers make it now possible to simulate (3+1)-dimensional pulses with broad (cm) waist over long ranges. These require fine enough resolution and the use of massively parallel machines with near-Terabyte memory storage. To the best of our knowledge, no numerical simulations restoring step by step multifilamented pulses clamped with long plasma channels have been published so far.

In this article, we model in full three-dimensional geometry the propagation of ultrashort pulses as reported from the Naval Research Laboratory experiments [8,9]. The experimental campaign which relied on a nondestructive technique for filament imaging allowed to follow the fluence patterns as the beam undergoes multifilamentation along the optical path. We display the fluence patterns whose filaments and location in the diffraction plane can be restored accurately by the numerical model at the same distances as in the experiments. This comparison together with the filament characterization is performed over almost 12 m for ultrashort pulses with 50 fs full width at half maximum (FWHM) duration, for which the magnitude of the nonlinear index is discussed. Influence of longer durations up to 450 fs on the evolution of the pulse profile is also addressed. We moreover demonstrate that the supercontinuum generated by a single filament is nearly identical with that emitted by a multitude of filaments at the same propagation distances.

*stephanie.champeaux@cea.fr

II. MODEL FOR FEMTOSECOND PULSE PROPAGATION

The standard model for atmospheric propagation of fs pulses couples the forward component of the laser field envelope $\mathcal{E}(x,y,z,t)$ with the electron density $\rho(x,y,z,t)$ through the following equations [10]:

$$i\frac{\partial}{\partial z}\mathcal{E} = -\frac{1}{2k_0}T^{-1}(\partial_x^2+\partial_y^2)\mathcal{E} - \hat{\mathcal{D}}\mathcal{E} - k_0 T\Delta n\mathcal{E} + \frac{k_0}{2\rho_c}T^{-1}\rho\mathcal{E} - i\frac{\sigma}{2}\rho\mathcal{E} - i\rho_{\mathrm{nt}}U_i\frac{W(I)}{2I}\mathcal{E}, \tag{1a}$$

$$\Delta n = n_2\left[(1-f)I + f\left(\frac{1+\omega_R^2\tau_{dk}^2}{\omega_R\tau_{dk}^2}\right)\int_{-\infty}^{t} e^{-(t-t')/\tau_{dk}} \times \sin[\omega_R(t-t')]I(t')dt'\right] - n_4 I^2, \tag{1b}$$

$$\frac{\partial}{\partial t}\rho = \rho_{\mathrm{nt}}W(I) + \frac{\sigma}{U_i}\rho I, \tag{1c}$$

where I stands for the field intensity $|\mathcal{E}|^2$, z is the propagation direction, t the retarded time in the frame moving with the group velocity, and $k_0=c/\omega_0=2\pi/\lambda_0$ denotes the central wave number for the laser wavelength $\lambda_0=800$ nm. The chromatic dispersion operator $\hat{\mathcal{D}}=\Sigma_{n\geqslant 2}^{n\leqslant 5}(k^{(n)}/n!)(i\partial_t)^n$ is treated in the Fourier domain where the coefficients $k^{(n)} \equiv \partial^n k/\partial\omega^n|_{\omega=\omega_0}$ are computed from Ref. [11]. Equation (1a) encompasses wave diffraction, chromatic dispersion, optical self-focusing, and plasma generation. Deviations from the slowly varying envelope approximation are self-consistently included through space time focusing $(T^{-1}\Delta_\perp\mathcal{E})$ and self-steepening $(T|\mathcal{E}|^2\mathcal{E})$. While bound electron anharmonicity induces instantaneous changes in the nonlinear optical refractive index (Kerr effect), inertial molecular dynamics responsible for stimulated rotational Raman scattering gives rise to a delayed Kerr contribution in ratio f [Eq. (1b)]. The latter reduces the Kerr self-focusing nonlinearity in front of the pulse, counteracts plasma defocusing of the pulse trailing edge, and may shift the spectral peak to larger wavelengths [6,12,13]. The fundamental rotational frequency and the characteristic relaxation time are respectively set to about $\omega_R\approx 1.6\times 10^{13}$ s^{-1} and $\tau_{\mathrm{dk}}\approx 77$ fs [14,15]. The delayed Kerr contribution is expected to only play a noticeable role for pulses with duration comparable or shorter than the characteristic Raman time scales ($\lesssim$100 fs). Unlike cw beams, the critical power for self-focusing of ultrashort pulses is no longer constant, but becomes time dependent as

$$P_{\mathrm{cr}} \equiv \lambda_0^2/2\pi n_2[1-f+f\mathcal{G}(t)], \tag{2}$$

where $\mathcal{G}(t)$ denotes the Raman integral of Eq. (1b) evaluated on the pulse temporal profile. This threshold decreases with long pulse durations $[\mathcal{G}(t)\to 1]$. Direct measurements based on the peak position of fluorescence signals as function of the pulse energy have shown that the critical power can double between long ($\geqslant$200 fs) and short (42 fs) pulses [16]. The nonlinear Kerr index n_2 and the ratio f may also depend on the pulse duration. The Kerr instantaneous and rotational Raman contribution to nonlinear index changes were experimentally and numerically found of same relative importance and measured about $n_2\approx 2.8-3\times 10^{-19}$ cm^2/W [6,15] with $f\approx 0.5$ at 800 nm for input pulse durations of 100–150 fs. For longer pulses $\geqslant$200 fs, the value $\approx 6\times 10^{-19}$ cm^2/W seems more appropriate [12,15]. We choose here to keep $f=0.5$ and to adjust the value of n_2 according to the input duration considered.

In air, free electrons are assumed to be mainly produced by photoionization of O_2 molecules whose ionization potential $U_i=12.1$ eV is lower than nitrogen's. The associated neutral density is $\rho_{\mathrm{nt}}=5.4\times 10^{18}$ cm^{-3}. The critical plasma density beyond which the beam can no longer propagate takes the value $\rho_c\approx 1.7\times 10^{21}$ cm^{-3} at 800 nm. The collisional ionization process with cross section $\sigma=5.46\times 10^{-20}$ cm^2 in Eq. (1c) plays a weaker role for ultrashort pulses (duration $<$1 ps) as atmosphere has low molecular density. Electron recombination which becomes efficient on long (ns) time scales is ignored. Several models with varying level of refinement are nowadays available to evaluate the photoionization rate $W(I)$ [17]. We shall opt for the model based on the Perelomov Popov Terent'ev theory (PPT) [18] which has been shown to provide a reliable description of self-guided propagation [17].

Besides plasma formation, quintic saturation arising from the expansion of the nonlinear polarization field can also contribute to the defocusing process [5]. The debate on how to discriminate ionization from the instantaneous saturation in the nonlinear responses is indeed still open [19]. However, multifilamentation dynamics has been shown to be better restored by considering quintic saturation, as filamentation patterns get stabilized and the energy losses reduced [20]. In particular it enables ones to retrieve the fusion of two spots into one lobe generically reported by experimentalists [21]. We here choose to discuss the dynamics of (3+1)-dimensional femtosecond filament with a weak coefficient $n_4\approx 2.5\times 10^{-33}$ cm^4/W^2 [5]. For completeness, the case without quintic saturation has also been simulated. It turns out that, because the n_4 coefficient is originally small, the results were altered to a little extent only. With quintic nonlinearities, a better accord with the experimental filamentation patterns is observed, while the discrepancies in the fluence maxima are slightly increased.

Because accurate comparisons between numerics and experiments need precise characterization of the filaments, a nondestructive technique for filament imaging [8] was used in the experiments. The diagnostic apparatus involved a helium chamber mounted on a table with guide rail which intercepted the filaments along the plasma range. As helium has lower nonlinear index and higher ionization potential than air, this technique allows us to directly measure the fluence distribution at several longitudinal positions, without either damaging the detection system or altering the filament profiles. The experiment [9] using this technique was entirely devoted to recording beam fluences step by step along the optical path. The peak fluence, energy and spot size of the brightest filaments were extracted from these measurements. The experimental setup delivered 50 fs and 450 fs pulses at the wavelength of 800 nm carrying about 20 mJ energy. The spatial profile was almost Gaussian with mean FWHM spot

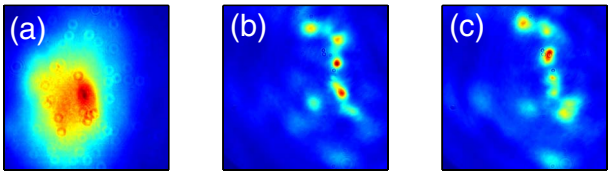

FIG. 1. (Color online) Experimental fluence distributions within an area of 5×5 mm^2 for the 50 fs pulse: (a) Initial profile at $z=0$ m and (b), (c) profiles recorded at $z=8.7$ m for two distinct shots.

size of 4–5 mm and quality factor $M^2\approx2.4$. The input beam profile of the 50 fs pulse is presented in Fig. 1(a).

To provide insight on the shot-to-shot stability of the recorded fluence pattern, five shots were taken at each longitudinal location considered. Figures 1(b) and 1(c) illustrate typical shot to shot fluctuations observed in multifilamentation regime at the longitudinal distance $z=8.7$ m reached by the 50 fs pulse. Basically, stability holds, in the sense that the number of filamentary sites and the gain lines along which they are observed are similar between several shots. Only the precise location and the brightness of the spots may vary.

The atmospheric propagation of ultrashort pulses is numerically investigated in full (3+1)-dimensional geometry. The above model is integrated by using a digitized file of the experimental input beam fluence shown in Fig. 1(a). A flat spatial phase is assumed together with a Gaussian temporal profile perturbed by 5% random noise. The input pulse is either fully compressed down to a FWHM duration of 50 fs or stretched to 450 fs by introducing a chirped phase e^{-iCt^2/t_p^2} with $C=8.94$ and $t_p=450/\sqrt{2\ln 2}$. It is worth noticing that only data issued from the 50 fs led to multiple filaments. Therefore, most of the analysis is devoted to this short pulse duration. Simulations were performed using a parallel spectral code running over 512 processors with minimal time and spatial steps of $\Delta t=0.5$ fs, $\Delta x=\Delta y=13$ μm, for an adaptative longitudinal step.

III. SPATIAL DYNAMICS

Reaching a quantitative agreement is always questionable. The multifilamentation regime makes it even harder to achieve. It is thus important to define the quantities that can provide suitable candidates for quantitative comparisons. Discrepancies are more likely to be observed on local quantities that often cumulate experimental error bars, such as maximal fluence, peak intensity, and electron density. Electron density and peak intensity are particularly sensitive. They indeed require the exact knowledge of the pulse temporal profile at given positions (x,y) and distances z, which was not accessible *in situ*. Electron densities, which were not diagnosed during the experimental campaign, are usually inferred from electric signals, acoustic or optical techniques, requiring integrated volumes (see reviews quoted in [1]). Therefore, quantitative comparisons are here restricted to directly measured data such as the beam fluence patterns. The fluence, energy, and waist of the brightest filaments are inferred from these measurements.

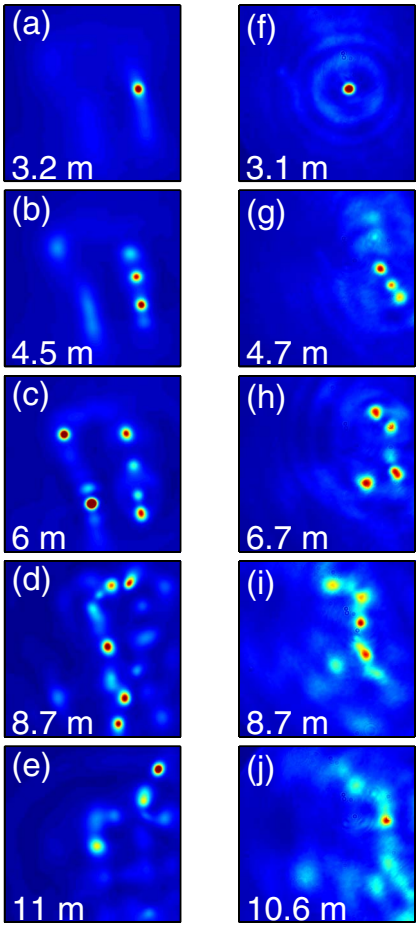

FIG. 2. (Color online) Fluence distributions within an area of 5×5 mm^2 for the 50 fs pulse: (a)–(e) Numerical results; (f)–(j) experimental data. Propagation distances are indicated inside the snapshots.

Figure 2 shows the fluence patterns formed by the 50 fs pulse at increasing propagation distances. The right-hand side column [Figs. 2(f)–2(j)] displays the experimental images. Starting from an almost Gaussian shape [see Fig. 1(a)], the beam self-focuses at $z_c\simeq3$ m leading first to the formation of a single filament at $z\approx3.1$ m. After nearly 1 m, the beam starts to break up. Additional filamenting sites arise till four cells get organized in a "trapezium" pattern at $z=4.7$ m. This pattern is unstable and becomes degraded by the occurrence of secondary cells resulting into 4–5 spots at $z\approx8.7$ m. The final image exhibits only one surviving filament at $z=10.6$ m. Numerical computations [Figs. 2(a)–2(e)] restore quite accurately the beam evolution in terms of nonlinear focus, number of filamentary cells and their relative location in the diffraction plane. The successive stages in the filamentation pattern evolution are faithfully reproduced. The longitudinal distances are almost identical to their experimental counterparts with maximal relative deviation of $\sim10\%$. Such remarkable agreement is achieved by selecting a nonlinear index n_2 equal to 2.5×10^{-19} cm^2/W. The effective critical power P_{cr} is thus assessed at about ~7 GW, which closely fits Liu and Chin's experimental results [16] for comparable pulse durations.

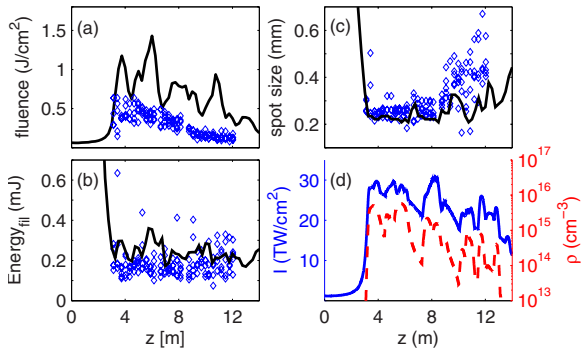

FIG. 3. (Color online) Numerical evolution along the propagation distance of the (a) peak fluence, (b) energy content of the brightest filament, (c) its FWHM spot size, and (d) the peak intensities (solid line) and peak electron densities (dashed line) associated with the 50 fs pulse; the experimental counterparts [9] (diamonds) are displayed on panels (a)–(c).

Figure 3 displays the characteristics of the brightest filaments predicted by the numerical computations superimposed with their experimental counterparts [9]. For completeness, levels reached by the peak electron density and peak intensity are numerically computed and indicated in the last panel [Fig. 3(d)]. The peak intensity stays clamped around 30 TW/cm^2 over nearly 6 m, with peak electron density as high as 5×10^{15} cm^{-3}. The peak fluence attains maxima oscillating between 0.6 and 1.4 J/cm^2 in the early filamentation stage and decreases afterward ($z>6$ m) to lower values around 0.3 J/cm^2 at 12 m. Its global behavior follows that exhibited by the experiment. The brightest filaments maintain an almost constant FWHM spot size of $\sim$240 μm over nearly 5 m, which is close to the experimental data with a mean spot size of $\sim$250 μm measured over the same propagation range. Following the procedure of [9], the energy content of the brightest filament is here defined for an integrating region that encompasses fluence values higher than 50% of the peak value. Numerics predict levels oscillating between $\sim$200 and 300 μJ versus an experimental mean value around 170 μJ. While the filament energy remains quasiconstant, the total energy (not shown here) keeps decreasing along the plasma range with an enhanced decay rate as the pulse breaks up into multiple filaments, accordingly to the experiment. Clearly, experimental and numerical filament characteristics closely match each other. Only differences in the observed and predicted peak fluence levels prevent us from achieving a full quantitative agreement. Such discrepancies might originate from combined effects such as uncertainty on measurements, calibration [8] and/or, as discussed above, on the choice of the quintic saturation coefficient for which we lack experimental data.

IV. TEMPORAL AND SPECTRAL DYNAMICS

A. Temporal evolution and influence of pulse duration

Figures 4(a) and 4(b) display typical temporal profiles computed numerically in the self-channeling regime. Beyond the nonlinear focus, the pulse maintains a self-compressed

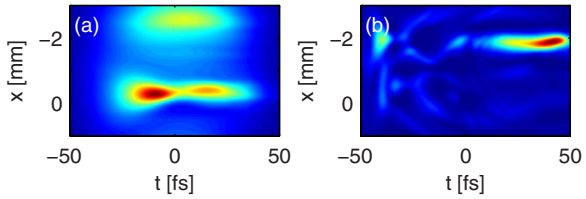

FIG. 4. (Color online) Spatiotemporal intensity patterns (at $y=0$ mm) computed for the 50 fs pulse at increasing propagation distances (a) $z=3.5$ m and (b) $z=8.7$ m.

shape with a temporal extent almost unaffected along the plasma range. The overall temporal duration remains of the order of a few tens of fs. Its small narrowing does not induce significant changes in the nonlinear refractive index. As a result only a slight increase of the effective critical power can be inferred, i.e., about 8 GW.

For comparison, we simulate the propagation of 450 fs pulses by selecting a higher intrinsic value of the Kerr index $n_2\approx6\times10^{-19}$ cm^2/W, in agreement with [12,15]. Delayed by the action of the positive chirp (the input power decreases by a factor $\sqrt{1+C^2}$), the beam self-focuses at a distance $z_c\approx6.5$ m which was found compatible with the experiments [9]. A single filament forms and stays stable upon much longer distances than for the 50 fs pulse. However, Fig. 5(a) reveals that near the nonlinear focus the pulse is compressed temporally to about $\sim$100 fs. This profile is maintained upon nearly 2 m. Unlike shorter pulses, the temporal narrowing of 450 fs pulses thus significantly affects the nonlinear refractive index: The effective critical power is assessed to increase from $\sim$1.7 GW to $\sim$2.5 GW. The inferred dependence of the effective critical power versus pulse duration is found consistent with experiments [16]. Further in the self-channeling regime, the pulse trail refocuses and undergoes optical shocks, shrinking the temporal extent down to a few tens of fs [Fig. 5(b)]. This property makes the initial value of the Kerr index $n_2\approx6\times10^{-19}$ cm^2/W inappropriate as duration becomes closer or less than 50 fs. Self-focusing and shock dynamics are artificially enhanced. As a result, simulations promoted a second filamentary cell arising from the amplification of an initial defect at around 3 m beyond z_c (not shown), whereas the experiment recorded a unique and stable filament over almost 6 m. Therefore, a fixed value of n_2 may not be compatible with long pulses that strongly evolve in time along the plasma range.

B. Spectral evolution

Figure 6 addresses the evolution of the power spectrum averaged over the entire simulation box. To carry on com-

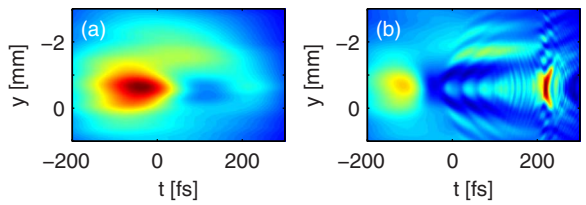

FIG. 5. (Color online) Spatiotemporal intensity patterns computed for the 450 fs pulse at increasing propagation distances (a) $z=6.5$ m and (b) $z=8.2$ m.

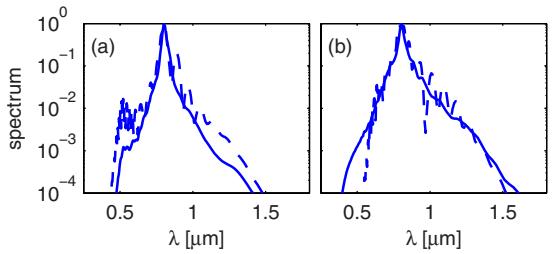

FIG. 6. (Color online) Averaged power spectra exhibited at (a) $z=7.75$ m and (b) $z=13$ m by the same multifilamenting beam as in Fig. 1 (solid line) and by a single filament arising from a 50 fs pulse carrying $\sim 4.6\ P_{cr}$ (dashed line).

parisons between spectra emitted either by multiple filaments or by a unique filament, a Gaussian pulse with a waist of 1.55 mm, same initial duration and power equal to 32 GW ($\sim 4.6\ P_{cr}$) is simulated using a radially symmetric code. The spectrum of the multifilamented beam builds up during the plasma self-channeling regime [see solid line of Fig. 6(a)], which ends at around 13 m once the peak electron density has fallen down to $10^{13}\ \mathrm{cm}^{-3}$ [Fig. 3(d)]. In the single-filamentation case, the plasma was shown to turn off at distance of ~ 8 m, from which the beam enters a postionization regime [22,23]. Beyond this point the infrared part of the spectrum remains almost unaffected while the blue one still develops as Kerr and shock dynamics are still active. After 13 m propagation, both spectra relax toward a similar shape. Comparison between the two spectral dynamics suggests that formation of multiple filaments both weakens the shock dynamics responsible for the spectral blueshift and smooths out the spectrum in the infrared range. Finally, the overall spectral distortions are found almost identical between a single filament and when the optical bundle supports the nucleation of several cells. This result is important. It demonstrates that the understanding of the white light generated by a powerful, optically turbulent beam can be captured by that emitted by an individual filament. This conclusion is consistent with the experimental observations of Chin *et al.* [24], following which two or more filaments emerge in phase from the background and possess the same phase relationship. This means that the laser spectrum around the central wavelength in the conditions for multiple filamentation is in principal identical to that developed by an isolated filament.

V. CONCLUSION

In summary, we numerically reproduced experimental propagation of a multifilamented beam with input duration of 50 fs in full (3+1)-dimensional geometry. For the first time to our knowledge, we have carried out a detailed quantitative comparison between numerical simulations and experimental measurements of filamentation over long distances in air. Many features, such as the number of filaments, their displacements inside the diffraction plane, their onset distances along the optical path, as well as several filament characteristics (fluence, energy, and waist) coincide with the experimental data. This ensures that Eqs. (1a)–(1c) capture the essential propagation physics to a point close to a complete "quantitative" accord. The inferred magnitude of the nonlinear Kerr index for the 50 fs pulse compares reasonably well with previous experimental evaluations [6,16]. The computations show that the spectrum follows the same dynamics in singly and multifilamentation regimes and thus exhibits a similar signature. The filamentation onset and early stage of filamentation dynamics can also be accurately reproduced for long pulses, using current and appropriate values of n_2. However, these pulses may undergo strong reduction of their temporal extent in self-channeling regime, which questions the validity of keeping a fixed Kerr index in the propagation models. In this regard, future work should address the issue of a self-consistent description of the nonlinear Kerr response along the optical path, as the pulse undergoes sharp temporal compression.

ACKNOWLEDGMENTS

Numerical computations were performed on the Bull cluster TERA10 of the CEA/DAM as part of the "Grands Challenges" program and on one of the HP clusters of the CCRT.

[1] A. Braun *et al.*, Opt. Lett. **20**, 73 (1995); E. T. J. Nibbering *et al.*, *ibid.* **21**, 62 (1996); H. R. Lange *et al.*, *ibid.* **23**, 120 (1998); B. LaFontaine *et al.*, Phys. Plasmas **6**, 1615 (1999); L. Wöste *et al.*, Laser Optoelektron. **29**, 51 (1997); see also, for review, L. Bergé *et al.*, Rep. Prog. Phys. **70**, 1633 (2007) and A. Couairon and A. Mysyrowicz, Phys. Rep. **441**, 47 (2007).
[2] J. H. Marburger, Prog. Quantum Electron. **4**, 35 (1975).
[3] M. Mlejnek, E. M. Wright, and J. V. Moloney, Opt. Lett. **23**, 382 (1998); P. Sprangle, J. R. Peñano, and B. Hafizi, Phys. Rev. E **66**, 046418 (2002).
[4] M. Rodriguez *et al.*, Phys. Rev. E **69**, 036607 (2004); J. Kasparian *et al.*, Science **301**, 61 (2003); M. Rodriguez *et al.*, Opt. Lett. **27**, 772 (2002).
[5] N. Aközbek *et al.*, Opt. Commun. **191**, 353 (2001).
[6] T. A. Pitts *et al.*, J. Opt. Soc. Am. B **21**, 112008 (2004).
[7] M. Mlejnek, M. Kolesik, J. V. Moloney, and E. M. Wright, Phys. Rev. Lett. **83**, 2938 (1999).
[8] A. Ting *et al.*, Appl. Opt. **44**, 1474 (2005).
[9] D. Gordon *et al.*, IEEE Trans. Plasma Sci. **34**, 249 (2006).
[10] S. Skupin and L. Bergé, Opt. Commun. **280**, 173 (2007).
[11] E. R. Peck and K. Reeder, J. Opt. Soc. Am. **62**, 958 (1972).
[12] J. R. Peñano, P. Sprangle, P. Serafim, B. Hafizi, and A. Ting, Phys. Rev. E **68**, 056502 (2003).
[13] M. Nurhuda and E. van Groesen, Phys. Rev. E **71**, 066502 (2005).
[14] J.-F. Ripoche *et al.*, Opt. Commun. **135**, 310 (1997).
[15] E. T. J. Nibbering *et al.*, J. Opt. Soc. Am. B **14**, 650 (1997).
[16] W. Liu and S. L. Chin, Opt. Express **13**, 5750 (2005).
[17] R. Nuter and L. Bergé, J. Opt. Soc. Am. B **23**, 874 (2006).
[18] A. M. Perelomov, V. S. Popov, and M. V. Terent'ev, Sov. Phys.

JETP **23**, 924 (1966).
[19] M. Nurhuda, A. Suda, and K. Midorikawa, Phys. Rev. A **66**, 041802(R) (2002).
[20] A. Vinçotte and L. Bergé, Phys. Rev. A **70**, 061802(R) (2004).
[21] S. Tzortzakis, L. Bergé, A. Couairon, M. Franco, B. Prade, and A. Mysyrowicz, Phys. Rev. Lett. **86**, 5470 (2001).
[22] S. Champeaux and L. Bergé, Phys. Rev. E **71**, 046604 (2005).
[23] S. Eisenmann, A. Pukhov, and A. Zigler, Phys. Rev. Lett. **98**, 155002 (2007).
[24] S. L. Chin *et al.*, Opt. Commun. **210**, 329 (2002).